Powder metallurgy of $Al_{0.1}CoCrFeNi$ high-entropy alloy

Rathinavelu Sokkalingam[1], Marek Tarraste[2], Kumar Babu Surreddi[3], Valdek Mikli[4], Veerappan Muthupandi[1], Katakam Sivaprasad[1,a), Konda Gokuldoss Prashanth[2,5,6,b)]

[1]Advanced Materials Processing Laboratory, Department of Metallurgical and Materials Engineering, National Institute of Technology, Tiruchirappalli 620015, Tamil Nadu, India
[2]Department of Mechanical and Industrial Engineering, Tallinn University of Technology, 19086 Tallinn, Estonia
[3]Materials Technology, Dalarna University, SE-791 88 Falun, Sweden
[4]Department of Materials and Environmental Technology, Tallinn University of Technology, 19086 Tallinn, Estonia
[5]Erich Schmid Institute of Materials Science, Austrian Academy of Sciences, Leoben A-8700, Austria
[6]CBCMT, School of Mechanical Engineering, Vellore Institute of Technology, Vellore 632014, India
a)Address all correspondence to these authors. e-mail: ksp@nitt.edu
b)e-mail: kgprashanth@gmail.com
Received: 30 April 2020; accepted: 9 September 2020

$Al_{0.1}CoCrFeNi$ high-entropy alloy (HEA) was synthesized successfully from elemental powders by mechanical alloying (MA) and subsequent consolidation by spark plasma sintering (SPS). The alloying behavior, microstructure, and mechanical properties of the HEA were assessed using X-ray diffraction, electron microscope, hardness, and compression tests. MA of the elemental powders for 8 h has resulted in a two-phased microstructure: α-fcc and β-bcc phases. On the other hand, the consolidated bulk $Al_{0.1}CoCrFeNi$-HEA sample reveals the presence of α-fcc and $Cr_{23}C_6$ phases. The metastable β-bcc transforms into a stable α-fcc during the SPS process due to the supply of thermal energy. The hardness of the consolidated bulk HEA samples is found to be 370 ± 50 $HV_{0.5}$, and the yield and ultimate compressive strengths are found to be 1420 and 1600 MPa, respectively. Such high strength in the $Al_{0.1}CoCrFeNi$ HEA is attributed to the grain refinement strengthening.

Introduction

The high-entropy alloy (HEA) concept is an innovative alloy design strategy, where multiple principal alloying elements are added (mostly in equiatomic proportions) to yield a single-phased microstructure [either face-centered-cubic (fcc) or body-centered-cubic (bcc)] [1, 2, 3]. Traditionally, the alloys contain a base principal element with minor alloying elements (mostly follow Hume–Rothery Rules) to achieve desired properties depending on their applications. It was strongly believed that alloying of more than one principal element could lead to the formation of intermetallic or complex structures or bulk metallic glasses [4, 5]. In 2004, Cantor and Yeh came up with new alloys, where multiple principle elements in equimolar fraction (CoCrFeMnNi and AlCoCrCuFeNi alloys) had resulted in a simple crystal structure [6, 7]. According to Yeh et al., the simple crystal structure attained in the HEA is attributed to the high configurational entropy of the system [6]. Further, HEAs exhibit superior mechanical properties, corrosion, oxidation, and irradiation resistance due to its intrinsic core effects like heavy lattice deformation and sluggish cooperative diffusion [8, 9, 10, 11, 12, 13, 14].

$Al_xCoCrFeNi$ HEA (alloy system with Co, Cr, Fe, and Ni added in equimolar ratio and "x" denotes the molar fraction of aluminum) is one of the prominent HEA system, which is extensively studied due to its varying crystal structure from fcc to bcc depending on the Al content [9]. The fcc based $Al_xCoCrFeNi$ HEA offers excellent strain rate sensitivities compared with the conventional crystalline fcc materials [9]. This alloy also exhibits high strength arising from the internal stresses which have large friction stress from lattice distortion, dislocation strengthening, and solid solution strengthening. $Al_xCoCrFeNi$-based HEAs exhibit a low stacking fault energy (SFE) <30 mJ/mm^2 [9, 10]. Such low SFEs hinder dynamic recovery thereby enhancing the dislocation storage capacity. This promotes the formation of deformation twins, which lead to high work hardening rates [9, 11, 12]. $Al_xCoCrFeNi$ HEAs show excellent structural stability [13] and mechanical properties [15, 16, 17, 18, 19, 20, 21] over the range of temperatures. Also, corrosion and wear resistance of $Al_xCoCrFeNi$ HEA is similar to the conventional alloys like AISI 304 stainless steel and Inconel 718 alloys [22, 23, 24]. Due to these excellent properties, extensive research has been carried out on $Al_xCoCrFeNi$-based HEAs.

However, most of the studies involve the production of the HEA *via* casting (arc melting/induction melting) route [13, 14, 15, 16, 17, 18, 19, 20, 22, 23, 24].

The strength of the Al_xCoCrFeNi HEA was found to be dependent on the Al concentration since it promotes and stabilizes a *bcc* structure [9, 13, 15, 17, 18, 20, 22]. Accordingly, $Al_{0.1}$CoCrFeNi HEA (A-HEA) is an excellent composition exhibiting a single *fcc* crystal structure [10, 12, 19, 25, 26]. The alloys are highly resistant to radiation [27, 28], high-temperature softening [13], and corrosion [29] compared with the conventional structural alloys. Even though A-HEA illustrates a unique work hardening behavior, the main drawback is its low yield strength (150 MPa) [25]. Yield strength indicates the upper-threshold value of the stress, after which the material could start to deform permanently its shape. The materials used in the structural parts need to withstand load for a long period under static as well as dynamic loading conditions; hence, the structures are usually designed in reference to the yield strength of the material to provide safe and reliable design [30]. Lower yield strength could limit the application of A-HEA; hence, the present work focuses on the strength improvement in A-HEA by tailoring its strengthening mechanisms [31, 32, 33, 34, 35, 36, 37, 38, 39, 40, 41]. Strengthening of alloys with the *fcc* phase can be achieved by either grain refinement [31, 32, 33, 34, 35, 36] or by dispersion strengthening (adding hard particles in the matrix) [37, 38, 39, 40, 41]. Grain refinement is one of the effective strengthening strategies that can be achieved in two ways: (i) Changing the processing technique (employ processes with a high cooling rate like additive manufacturing or copper mold casting or melt spinning) [42, 43, 44, 45] or using non-equilibrium processing like the mechanical alloying (MA) [46, 47, 48] or (ii) Employing thermomechanical processes [25, 36, 49, 50, 51]. Mainly, A-HEA-based alloys were strengthened by thermomechanical processing like severe plastic deformation (processing with friction stir processing [25], high-pressure torsion [49], etc.). Kumar et al. have achieved a yield strength improvement of about 315 MPa by grain refinement (reduction from millimeter to micrometer-range sized grains) [25]. Similarly, Xu et al. on the other hand employed cryo-rolling to improve the yield strength of the HEA to about 800 MPa [36]. Nevertheless, all the above-mentioned improvements in strength were carried out on cast samples.

Powder metallurgy is another alternative route that can fabricate samples and at the same time can strengthen the sample in several ways including grain refinement, solid solution strengthening, and dislocation strengthening [52, 53, 54]. MA followed by powder consolidation is one of the traditional solid-state alloy synthesis processes used in the powder metallurgical approach. It involves alloying of elemental powders by ball milling (alloying of elements occurs due to cyclic welding and fracture phenomenon between alloying elemental powders) and subsequently consolidating the ball-milled powders by sintering them at high temperature [45, 53, 54]. By this process, a range of materials starting from supersaturated solid solutions, quasicrystals, amorphous alloys, nanomaterials, and intermetallic with nano-structures can be produced [46, 55, 56, 57, 58, 59, 60, 61]. Spark plasma sintering (SPS) is a field-assisted sintering technique, which can consolidate the powder material rapidly. The SPS process with a higher heating rate enables a higher densification rate with sluggish grain coarsening rate during sintering. Hence, the SPS technique efficiently produces fine-grained bulk samples without affecting intrinsic properties and structures (nano or submicron structure) of the powder [62, 63]. By utilizing the advantage of SPS combining with MA, the present study focuses on the processing of A-HEA, where the aim is to improve the strength of the alloy by non-equilibrium powder processing. The resultant microstructure and mechanical properties are studied in detail.

Results

Mechanically alloyed $Al_{0.1}$CoCrFeNi powder

The scanning electron microscope (SEM) images of the elemental powders (Al, Co, Cr, Fe, and Ni) are given in Figs. 1(a)–1(e). The particle size distribution of elemental powders measured by laser granulometry is provided in Fig. 1(f). All of the elemental powders have shown different shapes and sizes. Al and Fe possessed with droplet-shaped with D_v50 of 30 ± 15 and 41 ± 17 µm, respectively; Co has finer particles (15 ± 7 µm) with dendritic structure; Cr shows irregularly shaped particles (D_v50 of 24 ± 12 µm); Ni depicts tree sponge shaped structure with D_v50 of 22 ± 16 µm. Figures 2(a)–2(d) display the SEM images of the mechanically alloyed powder as a function of milling time. The elemental powder mixture after 2 h of milling shows the presence of irregularly shaped particles with an average size of 35 ± 12 µm. It may be carefully observed from the image [Fig. 2(a)] that some particles exhibit smooth fractured surfaces and others exhibit rough surfaces as a result of repeated welding and fracturing events that take place during MA [46, 62]. The smooth surface corresponds to the fracture event, and once they are welded, the surface becomes rough and irregular. As the isopropanol is used as a processing control agent (PCA), it reduces the cold welding event and enables more fracturing events, which leads to a drastic reduction in the size of the particles after 4 h of milling and the average size of the particles is observed to be 18 ± 4.3 µm. The particles are irregular in shape, and both smooth and rough surfaces are observed just like in the 2 h milled powder samples.

MA of the $Al_{0.1}$CoCrFeNi powder to 6 h leads to a marginal increase in the size of the powder particles, which may be attributed to the cold welding incidents that take place during MA [46, 62]. The average size of the powder particles is
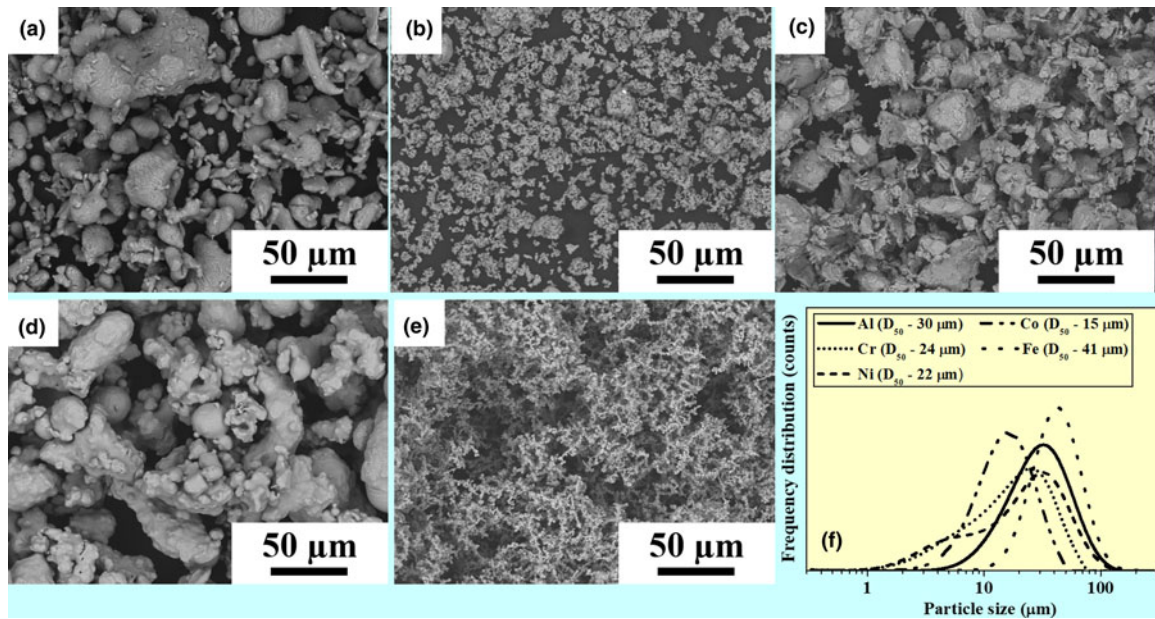
Figure 1: SEM images of the elemental powders: (a) Al, (b) Co, (c) Cr, (d) Fe, and (e) Ni, respectively, and (f) their corresponding particle size distribution.
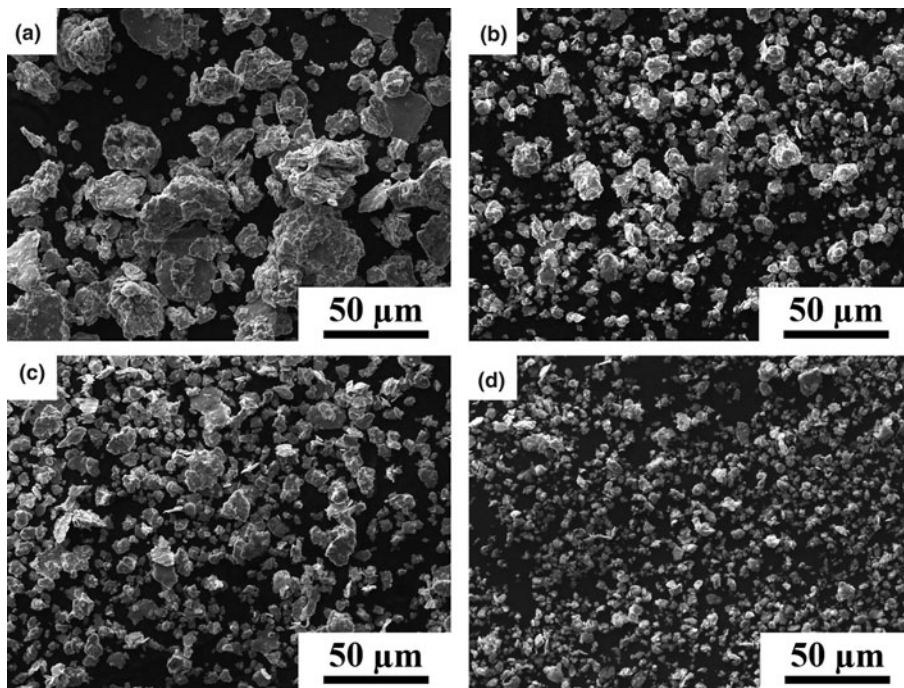

Figure 2: SEM images of the $Al_{0.1}CoCrFeNi$ elemental powders ball milled for (a) 2 h, (b) 4 h, (c) 6 h, and (d) 8 h, respectively.

observed to be $25 \pm 6.5 \mu m$. An increase in particle size indicates the predominant occurrence of the cold welding event and agglomeration of the powder particles after 6 h. The dominance of the welding event could occur in any one of the following conditions: (a) if the temperature of the milling medium reaches a certain critical temperature, PCA could not control the welding event effectively and leads to the agglomeration of the particles and (b) when the impact energy in the milling

process is not high enough to fracture the welded particles. With prolonged MA to 8 h, the size of the powder particles is drastically reduced, while maintaining the irregular shape. The average size of the $Al_{0.1}CoCrFeNi$ powder particles is observed to be $8 \pm 1.5 \mu m$. The size of the $Al_{0.1}CoCrFeNi$ HEA powders is drastically reduced from ~25 to 8 μm after 8 h of MA. Since the powder size is reduced drastically and there are several welding and fracturing events taking place
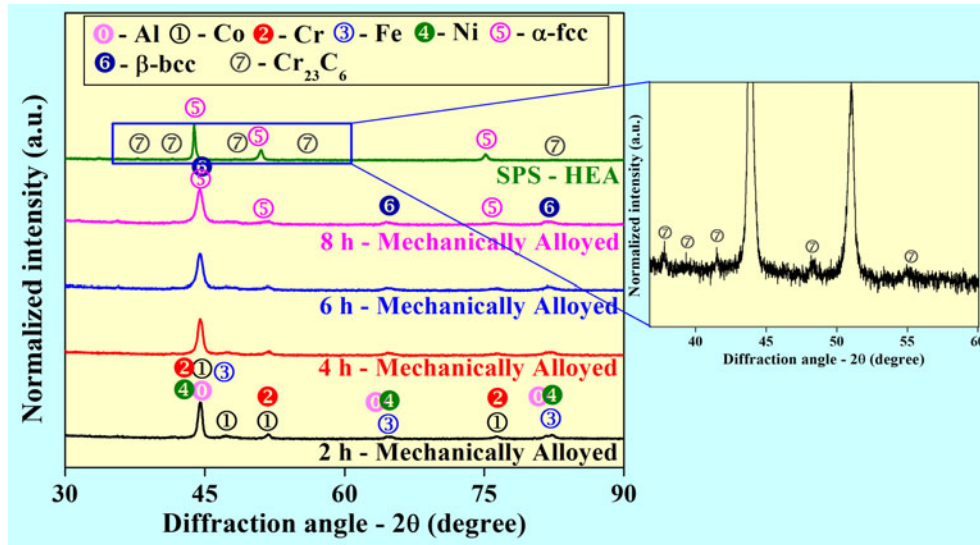
Figure 3: XRD patterns of the $Al_{0.1}CoCrFeNi$ HEA powders and spark-plasma sintered bulk sample.

due to the impact of ball and friction between them, the powder particles will be strained severely and the degree of internal stresses in the powder particles increases drastically with MA time, which may be measured using X-ray diffraction (XRD).

The XRD patterns of the MA $Al_{0.1}CoCrFeNi$ HEA powders (for 2, 4, 6, and 8 h, respectively) along with the SPS consolidated sample are shown in Fig. 3. The XRD pattern of the 2 h MA powder shows all the peaks corresponding to the elemental powders. However, with increasing the MA time, the identity of the individual elemental phases disappears, and the peaks corresponding to two crystal structures *fcc* and *bcc* are observed. The width of the peaks increases with increasing MA time, and this broadening may be attributed to the following factors: (i) decrease in the crystallite size or the coherent domain size, (ii) increase in the lattice strain or internal strain in the material, and (iii) increase in the number of internal defects like the dislocation density and stacking faults [64]. Besides, the peaks corresponding tend to shift toward a lower angle due to the alloying of the elements, eventually forming an alloy with high entropy in it. After 8 h of MA, peaks of only two crystal structures are observed: namely α-*fcc* and β-*bcc* phases, suggesting that the $Al_{0.1}CoCrFeNi$ HEA exhibits a two-phased crystal structure. The two-phased microstructure is the resultant of the formation of solid solutions during MA. Eventhough the single fcc phase was reported by other researchers [9, 10, 11, 12, 13, 14], in $Al_{0.1}CoCrFeNi$ HEA prepared by arc melting and induction melting techniques, $Al_{0.1}CoCrFeNi$ HEA prepared by MA shows the two-phased crystal structure. Such occurrence also observed during MA of CoCrFeMnNi HEA (which possesses a single *fcc* phase when prepared by arc melting and induction melting techniques) [61, 64].

The lattice parameter, crystalline size (D), and the lattice strain of the MA powders and the bulk SPS sample were evaluated from the XRD patterns by using the Williamson–Hall plot [65] and are tabulated in Table 1. The broadening of the peaks increases with increasing MA time implies that the crystallite size decreases, and the lattice strain increases because of the continuous hitting effect of the balls and vials during the MA process. The lattice parameter of the α-*fcc* phase increases with increasing MA time from 4 to 8 h (shift in the diffraction peaks to the lower angles) due to the expansion of the lattice with the diffusion of the elements. It may be observed from Table 1 that the crystallite size of both α-*fcc* and β-*bcc* phases decreases from 108 ± 10 to 37 ± 7 nm and 63 ± 6 to 8 ± 2 nm, respectively, when MA from 4 to 8 h. Similarly, the lattice strain increases constantly with an increase in the MA time.

The energy-dispersive X-ray (EDS) mapping of the A-HEA powder after 8 h of MA is given in Fig. 4. It can be observed that out of five principal alloying elements, Al, Co, Fe, and Ni are distributed evenly, whereas Cr is segregated along certain regions without having a uniform distribution like the other four elements. Among the metallurgical factors (atomic size, crystal size, melting point, and self-diffusing ability), the alloying ability was found to depend directly on mechanical disintegration and inversely on the melting point of the alloying elements [66]. In the present work, the reduction of particle size associated with the mechanical disintegration during MA has favored alloying of the elements. Chen et al. have reported that during alloying of the multi-principal elements (Al, Co, Cu, Cr, Fe, Mo, Ni, and Ti), the alloying rate of the elements decreases in the following order: Al→Cu→Co→Ni→Fe→Ti→Cr→Mo [66]. Similarly, in the present work, the alloying rate on the elements decreases in the following order: Al→Co→Ni→Fe→Cr. Since Cr has the least alloying rate among the five elements considered, it is segregated randomly. Additional thermal treatment or increasing

TABLE 1. The lattice parameter, crystallite size, and the lattice strain of the MA powders and the bulk $Al_{0.1}CoCrFeNi$ HEA samples calculated from the XRD patterns.

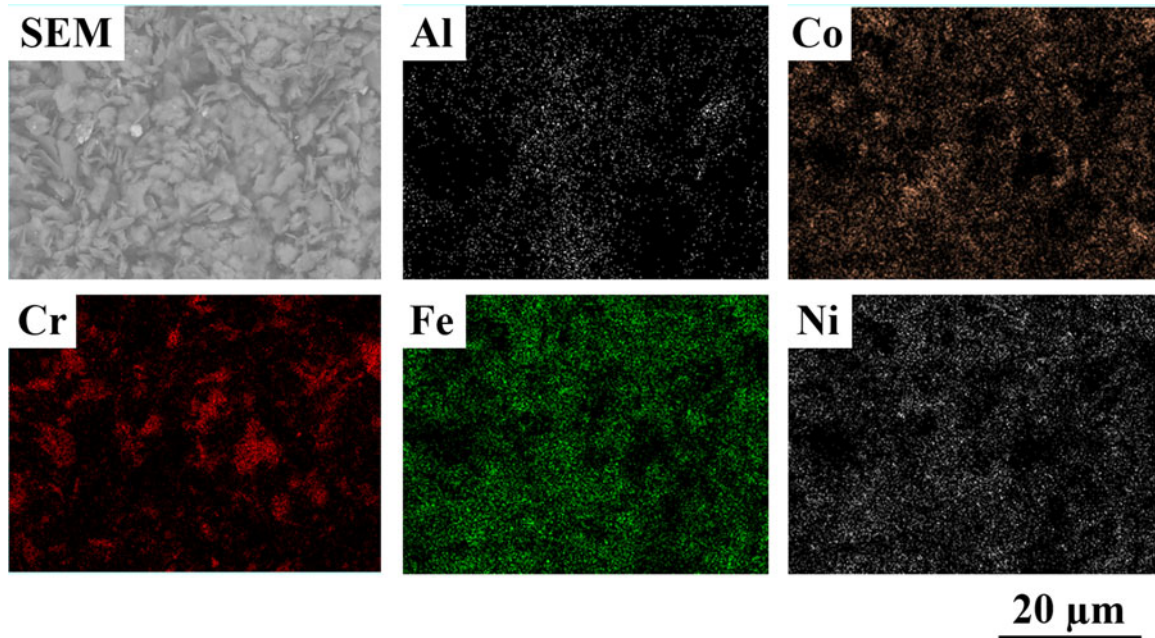| Sample designation	Lattice parameter (nm)		Crystalline size, D (nm)		Lattice strain ($\times 10^{-3}$)	
	α-phase	β-phase	α-phase	β-phase	α-phase	β-phase
4 h MA powder	0.3524 ± 0.0002	0.2875 ± 0.0002	108 ± 10	63 ± 6	6 ± 1	6 ± 2
6 h MA powder	0.3529 ± 0.0004	0.2876 ± 0.0001	82 ± 7	55 ± 8	7 ± 2	10 ± 1
8 h MA powder	0.3534 ± 0.0008	0.2878 ± 0.0004	37 ± 7	8 ± 2	5 ± 3	7 ± 0.5
Bulk $Al_{0.1}CoCrFeNi$ HEA	0.3572 ± 0.0003	–	48 ± 3	–	2 ± 1	–

Figure 4: Energy-dispersive X-ray elemental mapping of 8 h mechanical alloyed $Al_{0.1}CoCrFeNi$ HEA powder.

MA time may completely dissolve Cr in the HEA matrix; however, this is beyond the scope of the present manuscript.

Consolidated (spark plasma sintered) $Al_{0.1}CoCrFeNi$ HEA

The SPS consolidated A-HEA bulk sample show a density of 7.268 g/cc leading to a relative density of ~96% (calculated with respect to the density of A-HEA synthesized by the arc-melting furnace). The XRD pattern of the $Al_{0.1}CoCrFeNi$ bulk SPSed A-HEA sample (Fig. 3) shows the presence of two phases: α-fcc and $Cr_{23}C_6$-carbide phase. Interestingly, the β-bcc phase present in the 8 h MA powder disappears after the SPS process. The metastable β-bcc in the 8 h MA powder transforms into a stable α-fcc phase with the supply of thermal energy (atomic diffusion) during the SPS consolidation. In addition, peaks of the α-fcc shift toward the lower angle, and it influences the lattice parameter. The lattice parameter of the α-fcc phase in the bulk sample is observed to be 0.3572 nm, which is an increase of 0.0048 nm compared with the 8 h MA powder. Such an increase in lattice constant after SPS is due to the phase transformation from the metastable β-bcc phase into stable α-fcc phase and $Cr_{23}C_6$-carbide. In addition, the relaxation of the internal stress stored in MA powder also contributed to an increase in the lattice constant in SPSed A-HEA. It can be noted that the increase in the lattice parameter during MA is less compared with that of SPSed A-HEA. This is attributed to the pronounced phase transition in SPS consolidation than during MA due to the assistance of the thermal energy [64]. The crystallite size of the bulk HEA sample is ~48 nm, and the lattice strain is evaluated as 2×10^{-3} (no unit). The increase in the crystallite size (from 37 nm for the 8 h MA powder) and the decrease in the lattice strain (9×10^{-3} for the 8 h MA powder) after consolidation can be attributed to the supply of thermal energy to the powder during the SPS process, which helps the crystals to grow and the lattices to relax be giving up the internal strain in the material. Retainment of the nanometer-scale microstructure after SPS of A-HEA at 1000 °C is attributed to efficient heating of the powder [higher heating rate (100 °C)] and short holding time [62, 63].
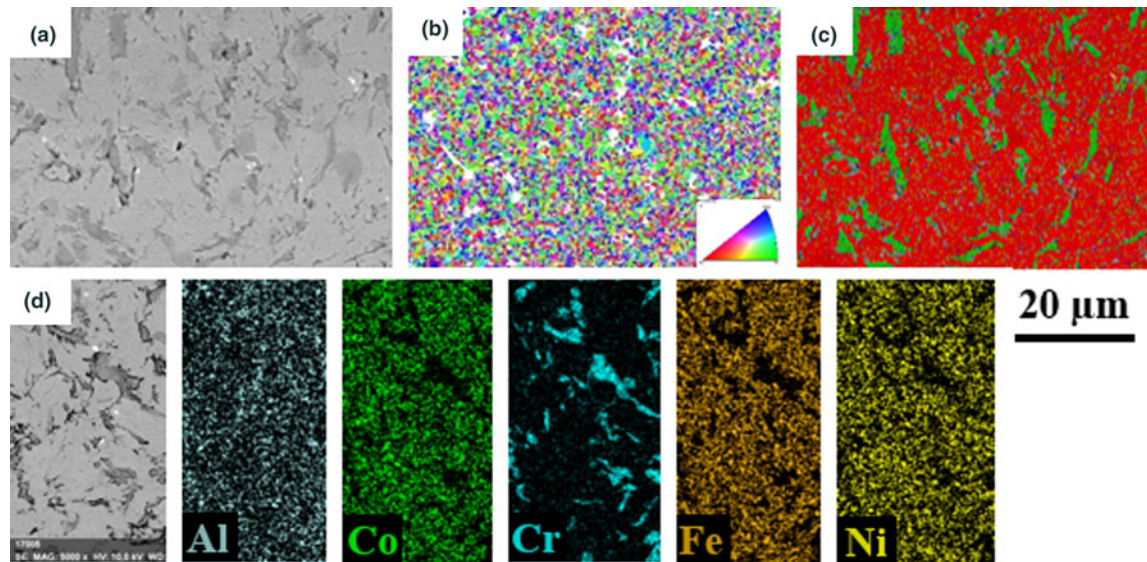
Figure 5: (a) SEM image of the spark plasma sintered bulk $Al_{0.1}CoCrFeNi$ HEA and the corresponding (b) EBSD image, (c) phase maps, and (d) EDS mapping images of the individual alloying elements (Al, Co, Cr, Fe, and Ni).

TABLE 2. Nominal chemical composition of the spark plasma sintered bulk $Al_{0.1}CoCrFeNi$ and their individual phases (at.%).

Description	Al	Co	Cr	Fe	Ni
Overall	1.63	24.44	25.39	24.65	22.78
Matrix	0.83	26.95	17.54	27.33	26.26
$Cr_{23}C_6$	2.01	13.71	56.78	14.86	11.69

The SEM, corresponding electron backscattered diffraction (EBSD) images, and phase maps of the bulk A-HEA sample are given in Fig. 5. The SEM image shows the presence of two different color contrasts in the microstructure, revealing the presence of two distinct phases (α-fcc and $Cr_{23}C_6$ phases) in Fig. 5(a). The EBSD image [Fig. 5(b)] shows the uniform distribution of nanocrystalline grains with an average size of ∼100 nm in the phases considered. Also, both the phases (α-fcc and $Cr_{23}C_6$ phases) are randomly oriented in the bulk sample. The phase map obtained from EBSD scan data [Fig. 5(c)] reveals that the red-colored phase corresponds to α-fcc phase and the green phase corresponds to the Cr-rich $Cr_{23}C_6$-phase. The fraction of $Cr_{23}C_6$ is measured as ∼14%. Further, the EDS area mapping [Fig. 5(d)] reveals the distribution of alloying elements in the bulk HEA sample. It can be observed that excepting Cr, all the elements (Al, Co, Fe, and Ni) have a uniform distribution throughout. The nominal composition of the alloy and the individual phases measured using EDS spot analysis are given in Table 2.

The α-phase with light contrast shows nearly equimolar distribution of the elements Co, Fe, and Ni and is deficient in Cr. On the other hand, the dark phase is rich in Cr. EDS spot analysis at $Cr_{23}C_6$ has the following composition: 56.78Cr–14.86Fe–11.69Ni–13.71Co–2.01Al (in at.%). The formation of $Cr_{23}C_6$ has been reported in the SPS processed HEAs containing

Cr such as $CoCrFeMnNiN_x$, AlCoCrFe, CoCrFeMnNi, and $Al_{0.3}CoCrFeMnNi$ HEAs. [67, 68, 69, 70, 71]. Vaidya et al. depicted the carbon contribution for carbide formation as the decomposition of the PCA [72]. Eventhough Cr-rich σ phase is reported in many literature [72], lower Gibb's free energy for chromium carbides than that of σ phase [73] has led to $Cr_{23}C_6$-carbide formation in the present investigation.

The bright-field transmission electron microscopy (TEM) images of the bulk HEA at the α-fcc matrix and at the interface between α-fcc matrix and $Cr_{23}C_6$ are shown in Figs. 6(a) and 6(b), respectively. Figure 6(a) reveals the presence of austenitic grains with twins indicating that the grains are in a recrystallized condition. The grains are distributed in the range of 50–200 nm. Whereas, the $Cr_{23}C_6$-phase is coarse-grained compared with the α-fcc matrix. Further, the $Cr_{23}C_6$-phase does not show any signs of twin formation. The interface between the α-fcc matrix and the $Cr_{23}C_6$-phase is coherent and epitaxially related to each other. The selected area diffraction (SAED) pattern of the matrix and Cr-rich-phase [Figs. 6(c) and 6(d)] reveals the presence of cubic (fcc) crystals and $Cr_{23}C_6$, respectively, corroborating with the XRD results. The presence of such an hard $Cr_{23}C_6$-phase is beneficial when present in minimum fraction. When the $Cr_{23}C_6$ fraction is increased, it could hamper the ductility of the material [74].

Mechanical properties of the bulk $Al_{0.1}CoCrFeNi$ HEA

The hardness of the bulk SPSed A-HEA sample is measured to be $370 \pm 50 \ HV_{0.5}$, which is almost double the value when compared with the hardness of their as-cast counterpart
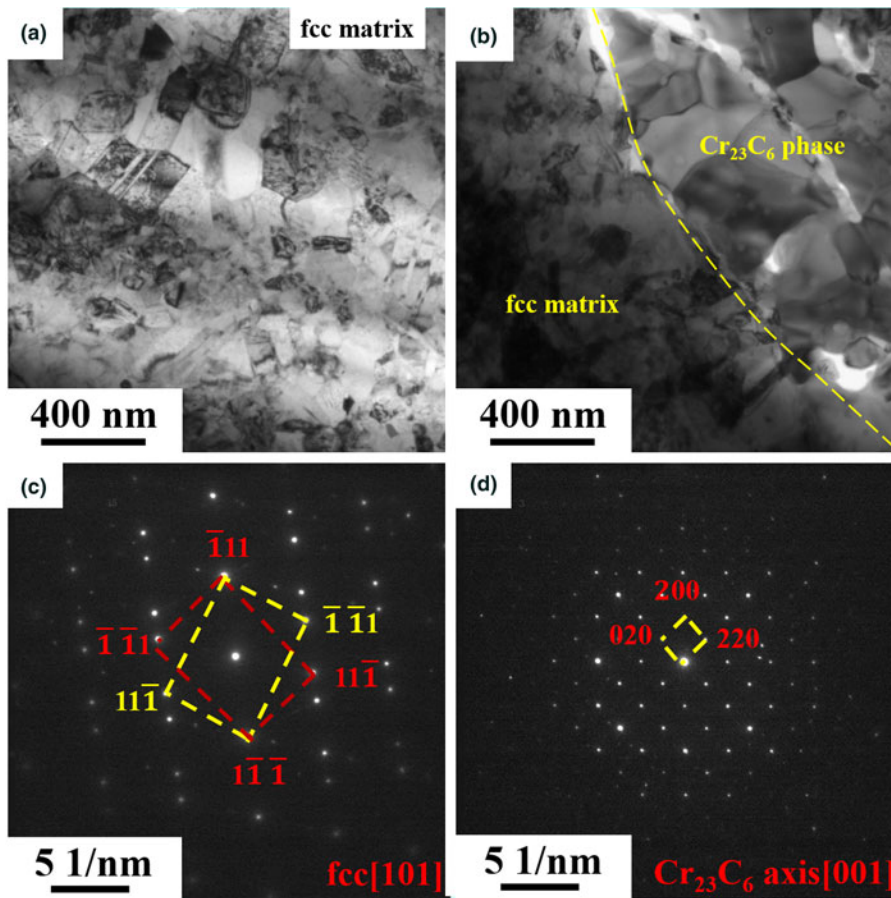
Figure 6: The bright-field TEM images of the spark plasma sintered bulk $Al_{0.1}CoCrFeNi$ HEA at the (a) α-fcc matrix and (b) interface between α-matrix and $Cr_{23}C_6$-carbide phase and (c and d) their corresponding SAED patterns.

(180 $HV_{0.5}$). Such an increase in the hardness of the samples may be attributed to the fine grain structure obtained during the MA process. The representative compressive stress–strain plot of the bulk HEA samples is illustrated in Fig. 7(a). The compressive yield strength (CYS) and ultimate compressive strength (UCS) for the bulk SPSed A-HEA were found to be 1420 ± 20 and 1600 ± 40 MPa, respectively, with plastic deformation of $10 \pm 2\%$. SPSed A-HEA shows seven-folds improvement in CYS and two-folds improvement in UCS of the A-HEA that prepared by vacuum arc melting and induction melting (CYS of $\sim$200 MPa and UCS of $\sim$900 MPa) [20]. Such enhancement in the CYS and UCS of A-HEA is attributable to the retainment of the nanometer-scale grains during SPS consolidation. This variation in strain may be attributed to the fraction of $Cr_{23}C_6$ particles/phase present in the sample used for the compression test. As Cr-rich phase only degrades the ductility of the sample, its fraction may lead to such variation. In addition, it may also be attributed to the differences in the defect levels in the samples like porosity.

Images of the fracture surface of the bulk HEA are shown in Figs. 7(b)–7(d). The brittle failure in the bulk HEA sample may be observed clearly from Fig. 7(b) in the form of cleavage (brittle facets). Higher magnification images show the presence of several microcracks, and some of them grow to form macrocracks, leading to the failure of the sample. Considering the phases present (α-fcc and the brittle $Cr_{23}C_6$) and the microstructural distribution of the phases, it may be attributed that the microcracks initiate from the brittle $Cr_{23}C_6$ when the local stress exceeds the fracture strength of the material. Several of such microcracks combine join together to form a macrocrack, leading to the failure of the material.

Discussion

The XRD analysis (Fig. 3) and micro to nano level structural characterization by electron microscopes (Figs. 5 and 6) have revealed that the SPS of A-HEA has resulted in the bulk A-HEA with dual-phase structure (with $\sim$86% α-fcc phase indicated in red color in the EBSD phase map and $\sim$14% $Cr_{23}C_6$-phase indicated in green color in the EBSD phase map). Further, it is noticeable that both the α-fcc phase and $Cr_{23}C_6$ phase retain nanocrystalline even after sintering at 1000 °C for 5 min using the SPS technique. The effective local heating of the powder surfaces by the higher heating rate (100 °C/min) in SPS restricts the grain coarsening during sintering and leads to effective sintering of the powders without
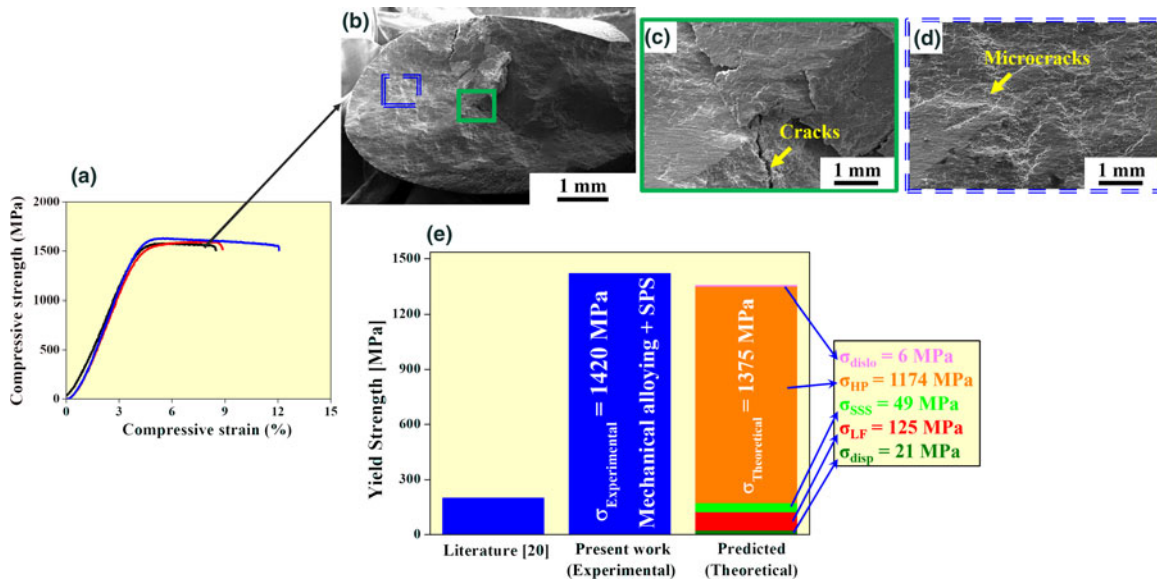
Figure 7: (a) Compressive stress–strain plot for the spark plasma sintered bulk $Al_{0.1}CoCrFeNi$ HEA and (b–d) secondary SEM images showing the fracture surface of the bulk $Al_{0.1}CoCrFeNi$ HEA samples after compression test. (e) Plot showing the experimental and theoretical strength of the bulk $Al_{0.1}CoCrFeNi$ HEA including the contributions from the various strengthening mechanisms.

altering the grain size of the powders. Whereas, A-HEA synthesized by vacuum arc melting and vacuum induction melting has revealed single α-fcc phase coarse grains in the range of millimeters at the as-cast condition and as-homogenized condition [20, 25, 26].

The hardness ($\sim$370 $HV_{0.5}$) and compressive strength (CYS: $\sim$1420 MPa and CUS: 1600 MPa) of the A-HEA prepared by SPS are higher than that of the as-cast/homogenized A-HEA prepared by vacuum arc melting and vacuum induction melting [20, 25, 26]. For engineering alloys, the yield strength can be dictated by the strengthening factors like intrinsic lattice friction (σ_{LF}), solid solution strengthening (σ_{SSS}), grain boundary strengthening/Hall–Petch strengthening (σ_{HP}), dislocation strengthening (σ_{dislo}), and particle dispersion strengthening (σ_{disp}). The yield strength of the alloy can be predicted by using the formula given in the following equation [75, 76, 77, 78, 79]:

$$\sigma_{Total} = \sigma_{LF} + \sigma_{SSS} + \sigma_{HP} + \sigma_{dislo} + \sigma_{disp}$$
$$= \sigma_o + \sigma_{HP} + \sigma_{dislo} + \sigma_{disp}, \quad (1)$$

$$\sigma_{LF} = \sum_{i=1}^{n} C_i * \sigma_{LR_i}, \quad (2)$$

where C_i and σ_{LR_i} are molar fraction and lattice friction stresses. Hence, σ_{LF} of the alloy is evaluated as 125.15 MPa by considering the lattice friction stresses of alloying elements; Al, Co, Cr, Fe, and Ni were reported as 16, 10.3, 454, 25, 22 MPa, respectively, from the recent publication [77]. Further, $\sigma_o = \sigma_{LF} + \sigma_{SSS}$ is a factor that includes lattice friction and solid solution strengthening contributions [75]. Kumar et al. have estimated the σ_o and Hall–

Petch coefficient (K_{HP}) for the $Al_{0.1}CoCrFeNi$ HEA as 174 and 371 MPa$(\mu m)^{1/2}$, respectively [25]. The remaining strength contributing factors (σ_{HP}, σ_{dislo}, and σ_{displ}) can be evaluated from Eqs. (3)–(5) [76].

$$\sigma_{HP} = \frac{K_{HP}}{\sqrt{d}}, \quad (3)$$

$$\sigma_{dislo} = M\alpha Gb\sqrt{\rho_{dislo}}, \quad (4)$$

$$\sigma_{disp} = \frac{M 0.4\, Gb}{\pi\lambda}\frac{\ln(2\bar{r}/b)}{\sqrt{1-\nu}}, \quad (5)$$

where d is the average grain size; M is the Taylor factor (3.06); α is the correlation factor for a specific material (0.2 for fcc materials), b is the Burgers vector, ρ_{dislo} is the dislocation density (calculated as 1.332×10^{17} m^{-2} from the XRD pattern), and L is inter-particle spacing calculated from

$$\lambda = 2\bar{r}\left(\sqrt{\frac{\pi}{4f}} - 1\right). \quad (6)$$

f is the volume fraction of particles, $\bar{r}$ is the average particle size of the dispersed particles, and ν is Poisson's ratio of the dispersed particles. The predicted strength values from σ_{HP}, σ_{dislo}, and σ_{disp} for the given bulk HEA sample are 1174, 6, and 21 MPa, respectively. Hence, total the yield strength of the bulk $Al_{0.1}CoCrFeNi$ HEA is estimated as 1375 MPa which suits well with the experimental yield strength (1420 MPa). The results show that the major strengthening mechanism operating in the bulk HEA sample is grain refinement strengthening [Fig. 7(e)],
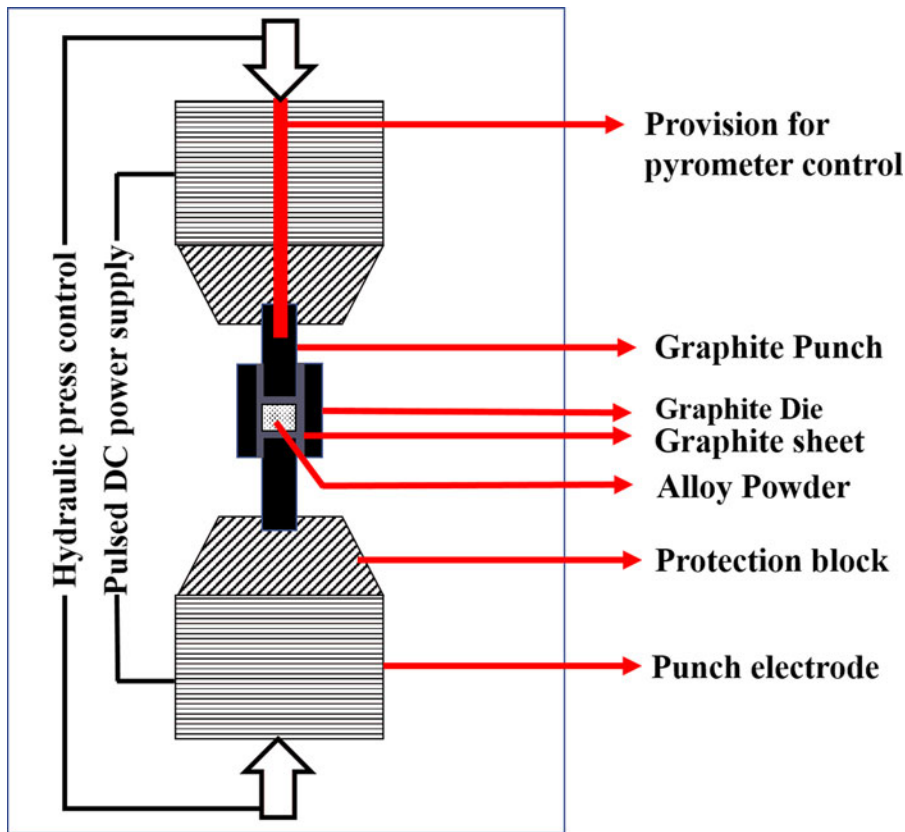
Figure 8: Schematic illustration showing the SPS setup.

which is attributed to the MA process. Such grain refinement strengthening is absent in the cast materials, excepting thermo-mechanical treatments are carried out after fabrication.

Even though the strength of the bulk $Al_{0.1}CoCrFeNi$ HEA is improved significantly by MA and subsequent SPS, the fracture strain of the materials is decreased drastically to ~10 ± 2%. This may be attributed to the presence of $Cr_{23}C_6$ (which is brittle) and is distributed unevenly in the α-fcc matrix.

Summary

Processing of bulk $Al_{0.1}CoCrFeNi$ HEA through powder metal-lurgy route (MA combined with SPS) was studied in detail. The following summary may be drawn.

(1) MA of the $Al_{0.1}CoCrFeNi$ elemental powders for 8 h has resulted in a two-phased microstructure: α-fcc and β-bcc phases.
(2) The consolidation of the powders *via* SPS has led to a phase transformation, where the metastable β-bcc phase transforms into a stable α-fcc phase. In addition, brittle $Cr_{23}C_6$ is present in the α-fcc matrix.
(3) The hardness of the bulk $Al_{0.1}CoCrFeNi$ HEA was found to be 370 ± 50 $HV_{0.5}$. CYS of 1420 MPa and compressive ultimate strength of 1600 MPa were observed along with a

plastic strain of ~10%. The strength is significantly higher than the as-cast counterpart; however, the plastic strain is drastically reduced due to the presence of brittle $Cr_{23}C_6$. Such high strength is attributed predominantly to the strengthening of the material by grain refinement, which is obtained through the MA process.

Materials and Methods

Material synthesis

40 g of pure (99.9%) Al, Co, Cr, Fe, and Ni metal powders were taken with the molar ratio of 0.1:1:1:1:1. The particle size of the elemental powders was measured using Analysette 22 COMPACT device (Fraunhofer approximation) from Fritsch GmbH, Idar-Oberstein, Germany. The powder mixer was mechanically alloyed using a high-energy planetary mill (RETSCH Emax, Haan, Germany). WC-Co balls with an average diameter of 5 mm were used. The ball to powder ratio was kept as 5:1, and the MA was carried out at 1500 rpm for 8 h. The vials were made of WC. To study the alloying behavior, the powders were sampled at regular intervals (2, 4, 6, and 8 h). To prevent the metal powders from bonding together and to avoid the sharp temperature rise during MA, isopropa-nol has been used as the process control agent. The powders after 8 h of MA were used for the consolidation process.

The schematic of powder consolidation/sintering by the SPS process is given in Fig. 8. Graphite die/punch setup with 20 mm diameter, shielded with graphite sheet was filled with mechanically alloyed $Al_{0.1}CoCrFeNi$ HEA. Then, the packed powders were sintered using SPS (HPD 10-GB from FCT Systeme GmbH, Frankenblick, Germany). The temperature used for sintering was 1000 °C with an applied pressure of 50 MPa for 5 min. The required temperature for sintering was achieved at a heating rate of 100 °C/min. The entire SPS operation was carried out under argon atmosphere inside a glove box. Finally, the surface of the bulk $Al_{0.1}CoCrFeNi$ HEA sample after sintering was machined to remove any possible contamination (like carbon) on the surface of the material.

Characterization and testing

The bulk $Al_{0.1}CoCrFeNi$ HEA was polished as per the ASTM E3 standard for further characterization. Structural characterization of the powder and the bulk samples were carried out using the X-ray diffractometer from Rigaku, Neu-Isenburg, Germany (UltimaIII). X-ray diffractometer operated with Cu K_α radiation (with X-ray wavelength:1.5406 Å) was used to scan the samples between 30° and 90° with a step size of 0.05°. The microstructure of the powders and bulk sample was recorded using a Zeiss field emission gun scanning electron microscope (FEG-SEM). The EBSD analysis and energy-dispersive X-ray spectroscopy (EDS) analysis were done to evaluate the microtexture and chemical composition analysis using Quanta-3D FEG-SEM equipped with a TSL-OIM EBSD unit. Bright-field images and the SAED patterns were recorded using TEM from Tecnai G2 F20, FEI, Boon, Germany. The density of the bulk HEA samples was evaluated using the Archimedes principle. The Vickers microhardness measurements were carried out according to the ASTM E384 standard, using the MICRO MET 2001 device (Buehler GmbH, Braunswick, Germany) with a load of 500 g and a dwell time of 10 s. The compression test samples of dimensions: 3.5 mm diameter and 7 mm height (H/D ratio = 1.5) were extracted from the bulk SPS sample as per the ASTM E9 standard. The compression test was carried out with a strain rate of 10^{-3}/s using the INSTRON 5569 machine, Darmstadt, Germany.

Acknowledgments

References

1. **E.P. George, D. Raabe, and R.O. Ritchie**: High-entropy alloys. *Nat. Rev. Mater.* **4**, 515 (2019).

2. **E.P. George, W.A. Curtin, and C.C. Tasan**: High entropy alloys: A focused review of mechanical properties and deformation mechanisms. *Acta Mater.* **188**, 435 (2020).

3. **D.B. Miracle and O.N. Senkov**: A critical review of high entropy alloys and related concepts. *Acta Mater.* **122**, 448 (2017).

4. **D.B. Miracle, J.D. Miller, O.N. Senkov, C. Woodward, M.D. Uchic, and J. Tiley**: Exploration and development of high entropy alloys for structural applications. *Entropy* **16**, 494 (2014).

5. **R. Sokkalingam, K. Sivaprasad, M. Duraiselvam, V. Muthupandi, and K.G. Prashanth**: Novel welding of $Al_{0.5}CoCrFeNi$ high-entropy alloy: Corrosion behavior. *J. Alloys Compd.* **817**, 153163 (2020).

6. **J.W. Yeh, S.K. Chen, S.J. Lin, J.Y. Gan, T.S. Chin, T.T. Shun, C.H. Tsau, and S.Y. Chang**: Nanostructured high-entropy alloys with multiple principal elements: Novel alloy design concepts and outcomes. *Adv. Eng. Mater.* **6**, 299 (2004).

7. **B. Cantor, I.T.H. Chang, P. Knight, and A.J.B. Vincent**: Microstructural development in equiatomic multicomponent alloys. *Mater. Sci. Eng. A* **375**, 213 (2004).

8. **C. Sajithbabu, K. Sivaprasad, V. Muthupandi, and J.A. Szpunar**: Characterization of nanocrystalline AlCoCrCuNiFeZn high entropy alloy produced by mechanical alloying. *Procedia Mater. Sci.* **5**, 1020 (2014).

9. **S. Gangireddy, B. Gwalani, V. Soni, R. Banerjee, and R.S. Mishra**: Contrasting mechanical behavior in precipitation hardenable $Al_xCoCrFeNi$ high entropy alloy microstructures: Single phase FCC vs. dual phase FCC-BCC. *Mater. Sci. Eng. A* **739**, 158 (2019).

10. **N. Kumar, Q. Yinh, X. Nie, R.S. Mishra, Z. Tang, P.K. Liaw, R.E. Brennan, K.J. Dohetry, and K.C. Cho**: High strain-rate compressive deformation behavior of $Al_{0.1}CrFeCoNi$ high entropy alloy. *Mater. Des.* **86**, 598 (2015).

11. **S. Gangireddy, B. Gwalani, K. Liu, R. Banerjee, and R.S. Mishra**: Microstructures with extraordinary dynamic work hardening and strain rate sensitivity in $Al_{0.3}CoCrFeNi$ high entropy alloy. *Mater. Sci. Eng. A* **734**, 42 (2018).

12. **S. Gangireddy, L. Kaimiao, B. Gwalani, and R.S. Mishra**: Microstructural dependence of strain rate sensitivity in thermomechanically processed $Al_{0.1}CoCrFeNi$ high entropy alloy. *Mater. Sci. Eng. A* **727**, 148 (2018).

13. **W.R. Wang, W.L. Wang, and J.W. Yeh**: Phases, microstructure and mechanical properties of $Al_xCoCrFeNi$ high-entropy alloys at elevated temperatures. *J. Alloys Compd.* **589**, 143 (2014).

14. **B. Gludovatz, A. Hohenwarter, D. Catoor, E.H. Chang, E.P. George, and R.O. Ritchie**: A fracture-resistant high-entropy alloy for cryogenic applications. *Science* **345**, 1153 (2014).

15. **C.J. Tong, M.R. Chen, J.W. Yeh, S.J. Lin, S.K. Chen, T.T. Shun, and S.Y. Chang**: Mechanical performance of the $Al_xCoCrCuFeNi$

high-entropy alloy system with multiprincipal elements. *Metall. Mater. Trans. A* **36**, 1263 (2005).

16. R. Sokkalingam, S. Mishra, S.R. Cheethirala, V. Muthupandi, and K. Sivaprasad: Enhanced relative slip distance in gas-tungsten-arc-welded $Al_{0.5}CoCrFeNi$ high-entropy alloy. *Metall. Mater. Trans. A* **48**, 3630 (2017).

17. D.Y. Li and Y. Zhang: The ultrahigh charpy impact toughness of forged $Al_xCoCrFeNi$ high entropy alloys at room and cryogenic temperatures. *Intermetallics* **70**, 24 (2016).

18. Y. Sun, P. Chen, L. Liu, M. Yan, X. Wu, C. Yu, and Z. Liu: Local mechanical properties of $Al_xCoCrCuFeNi$ high entropy alloy characterized using nanoindentation. *Intermetallics* **93**, 85 (2018).

19. R. Sokkalingam, V. Muthupandi, K. Sivaprasad, and K.G. Prashanth: Dissimilar welding of $Al_{0.1}CoCrFeNi$ high-entropy alloy and AISI304 stainless steel. *J. Mater. Res.* **34**, 2683 (2019).

20. Y. Lv, R. Hu, Z. Yao, J. Chen, D. Xu, Y. Liu, and X. Fan: Cooling rate effect on microstructure and mechanical properties of $Al_xCoCrFeNi$ high entropy alloys. *Mater. Des.* **132**, 292 (2017).

21. J. Karimi, P. Ma, Y.D. Jia, and K.G. Prashanth: Linear patterning of high entropy alloy by additive manufacturing. *Manuf. Lett.* **24**, 9 (2020).

22. Y. Shi, L. Collins, R. Feng, C. Zhang, N. Balke, P.K. Liaw, and B. Yang: Homogenization of $Al_xCoCrFeNi$ high-entropy alloys with improved corrosion resistance. *Corr. Sci.* **133**, 120 (2018).

23. R. Sokkalingam, K. Sivaprasad, M. Duraiselvam, V. Muthupandi, and K.G. Prashanth: Novel welding of $Al_{0.5}CoCrFeNi$ high-entropy alloy: Corrosion behavior. *J. Alloys Compd.* **817**, 153163 (2020).

24. J. Joseph, N. Haghdadi, K. Shamlaye, P. Hodgson, M. Barnett, and D. Fabijanic: The sliding wear behaviour of CoCrFeMnNi and $Al_xCoCrFeNi$ high entropy alloys at elevated temperatures. *Wear* **428–429**, 32 (2019).

25. N. Kumar, M. Komarasamy, P. Nelaturu, Z. Tang, P.K. Liaw, and R.S. Mishra: Friction stir processing of a high entropy alloy $Al_{0.1}CoCrFeNi$. *JOM* **67**, 1007 (2015).

26. R. Sokkalingam, P. Mastanaiah, V. Muthupandi, K. Sivaprasad, and K.G. Prashanth: Electron beam welding of high entropy alloy and stainless steel: Microstructure and mechanical properties. *Mater. Manuf. Process.* (2020). doi: 10.1080/10426914.2020.1802045

27. S.Q. Xia, X. Yang, T.F. Yang, S. Liu, and Y. Zhang: Irradiation resistance in $Al_xCoCrFeNi$ high entropy alloys. *JOM* **67**, 2340 (2015).

28. T. Yang, S. Xia, S. Liu, C. Wang, S. Liu, Y. Fang, Y. Zhang, J. Xue, S. Yan, and Y. Wang: Precipitation behavior of $Al_xCoCrFeNi$ high entropy alloys under ion irradiation. *Sci. Rep.* **6**, 32146 (2016).

29. R.B. Nair, H.S. Arora, S. Mukherjee, S. Singh, H. Singh, and H.S. Grewal: Exceptionally high cavitation erosion and corrosion resistance of a high entropy alloy. *Ultrason. Sonochem.* **41**, 252 (2018).

30. R. Li, J. Hou, W. Yang, H. Yu, Q. Wang, and Z. Zhang: Strengthening mechanism and yield strength prediction of cold-drawn commercially pure aluminum wire. *IOP Conf. Ser. Mater. Sci. Eng.* **382**, 022094 (2018).

31. S.W. Wu, G. Wang, J. Yi, Y.D. Jia, I. Hussain, Q.J. Zhai, and P.K. Liaw: Strong grain-size effect on deformation twinning of an $Al_{0.1}CoCrFeNi$ high-entropy alloy. *Mater. Res. Lett.* **5**, 276 (2017).

32. Z. Fu, W. Chen, H. Wen, D. Zhang, Z. Chen, B. Zheng, Y. Zhou, and E.J. Lavernia: Microstructure and strengthening mechanisms in an FCC structured single-phase nanocrystalline $Co_{25}Ni_{25}Fe_{25}Al_{7.5}Cu_{17.5}$ high-entropy alloy. *Acta Mater.* **107**, 59 (2016).

33. Z. Wang, R.T. Qu, S. Scudino, B.A. Sun, K.G. Prashanth, D.V. Louzguine-Luzgin, M.W. Chen, Z.F. Zhang, and J. Eckert: Hybrid nanostructured aluminum alloy with super-high strength. *NPG Asia Mater.* **7**, e229 (2015).

34. T. Maity, K.G. Prashanth, O. Balci, J.T. Kim, T. Schoeberl, Z. Wang, and J. Eckert: Influence of severe straining and strain rate on the evolution of dislocation structures during micro-/nanoindentatoin in high entropy lamellar eutectics. *Int. J. Plasticity* **109**, 121 (2018).

35. K.G. Prashanth, S. Scudino, H.J. Klauss, K.B. Surreddi, L. Loeber, Z. Wang, A.K. Chaubey, U. Kuehn, and J. Eckert: Microstructure and mechanical properties of Al-12Si produced by selective laser melting: Effect of heat treatment. *Mater. Sci. Eng. A* **590**, 153 (2014).

36. X.D. Xu, P. Liu, A. Hirata, S.X. Song, T.G. Nieh, and M.W. Chen: Microstructural origins for a strong and ductile $Al_{0.1}CoCrFeNi$ high-entropy alloy with ultrafine grains. *Materialia* **4**, 395 (2018).

37. Z. Wang, J. Tan, S. Scudino, B.A. Sun, R.T. Qu, J. He, K.G. Prashanth, W.W. Zhang, Y.Y. Li, and J. Eckert: Mechanical behavior of Al-based matrix composites reinforced with $Mg_{58}Cu_{28.5}Gd_{11}Ag_{2.5}$ metallic glass. *Adv. Powder Technol.* **25**, 635 (2014).

38. Z. Wang, K.G. Prashanth, S. Scudino, A.K. Chaubey, D.J. Sordelet, W.W. Zhang, Y.Y. Li, and J. Eckert: Tensile properties of Al matrix composites reinforced with in situ devitrified $Al_{84}Gd_6Ni_7Co_3$ glassy particles. *J. Alloys Compd.* **586**, S419 (2014).

39. F. Ali, S. Scudino, G. Liu, V.C. Srivastava, N.K. Mukhopadhyay, M. Samadi Khoshkhoo, K.G. Prashanth, V. Uhlenwinkel, M. Calin, and J. Eckert: Modeling the strengthening effect of Al–Cu–Fe quasicrystalline particles in Al-based metal matrix composites. *J. Alloys Compd.* **536S**, S130 (2012).

40. K.G. Prashanth, S. Scudino, A.K. Chaubey, L. Loeber, P. Wang, H. Attar, F.P. Schimansky, F. Pyczak, and J. Eckert: Processing of

Al-12Si-TNM composites by selective laser melting and evaluation of compressive and wear properties. *J. Mater. Res.* **31**, 55 (2016).

41. N. Singh, S. Banerjee, O. Parkash, and D. Kumar: Tribological and corrosion behavior of $(100-x)(Fe_{70}Ni_{30})-(x)ZrO_2$ composites synthesized by powder metallurgy. *Mater. Chem. Phys.* **205**, 261 (2018).

42. K.G. Prashanth, S. Scudino, and J. Eckert: Defining the tensile properties of Al-12Si parts produced by selective laser melting. *Acta Mater.* **126**, 25 (2017).

43. K.G. Prashanth, S. Kolla, and J. Eckert: Additive manufacturing processes: Selective laser melting, electron beam melting and binder jetting—selection guidelines. *Materials* **10**, 672 (2017).

44. K.G. Prashanth, H. Shakur Shahabi, H. Attar, V.C. Srivastava, N. Ellendt, V. Uhlenwinkel, J. Eckert, and S. Scudino: Production of high strength $Al_{85}Nd_8Ni_5Co_2$ alloy by selective laser melting. *Addit. Manuf.* **6**, 1 (2015).

45. N. Singh, R. Ummethala, P. Hameed, R. Sokkalingam, and K.G. Prashanth: Competition between densification and microstructure of functional materials by selective laser melting. *Mater. Des. Process. Comm.* **2**, e146 (2020).

46. C. Suryanarayana: Mechanical alloying and milling. *Prog. Mater. Sci.* **46**, 1 (2001).

47. K.G. Prashanth: Influence of mechanical activation on decomposition of titanium hydride. *Mater. Manuf. Process.* **25**, 974 (2010).

48. Z. Wang, K.G. Prashanth, S. Scudino, J. He, W.W. Zhang, Y.Y. Li, M. Soica, G. Vaughan, D.J. Sordelet, and J. Eckert: Effect of ball milling on structure and thermal stability of $Al_{84}Gd_6Ni_7Co_3$ glassy powders. *Intermetallics* **46**, 97 (2014).

49. T. Maity, K.G. Prashanth, A. Janda, J.T. Kim, F. Spieckermann, and J. Eckert: Mechanism of high-pressure torsion-induced shear banding and lamellar thickness saturation in Co–Cr–Fe–Ni–Ng high-entropy composites. *J. Mater. Res.* **34**, 2672 (2019).

50. T. Maity, K.G. Prashanth, O. Balci, Z. Wang, Y.D. Jia, and J. Eckert: Plastic deformation mechanisms in severely strained eutectic high entropy composites explained via strain rate sensitivity and activation volume. *Comp. Part B* **150**, 7 (2018).

51. P.F. Yu, H. Cheng, L.J. Zhang, H. Zhang, Q. Jing, M.Z. Ma, P.K. Liaw, G. Lia, and R.P. Liu: Effects of high-pressure torsion on microstructures and properties of an $Al_{0.1}CoCrFeNi$ high-entropy alloy. *Mater. Sci. Eng. A* **655**, 283 (2016).

52. A.K. Chaubey, S. Scudino, K.G. Prashanth, and J. Eckert: Microstructure and mechanical properties of Mg–Al-based alloy modified with cerium. *Mater. Sci. Eng. A* **625**, 46 (2015).

53. E.Y. Gutmanas: Materials with fine microstructure by advanced powder metallurgy. *Prog. Mater. Sci.* **34**, 261 (1990).

54. D. Marko, K.G. Prashanth, S. Scudino, Z. Wang, N. Ellendt, V. Uhlenwinkel, and J. Eckert: Al-based metal matrix composites reinforced with $Fe_{49.9}Co_{35.1}Nb_{7.7}B_{4.5}Si_{2.8}$ glassy powder:

Mechanical behavior under tensile loading. *J. Alloys Compd.* **615**, S382 (2014).

55. A.K. Chaubey, S. Scudino, M.S. Khoshkhoo, K.G. Prashanth, N.K. Mukhopadhyay, B.K. Mishra, and J. Eckert: High-strength ultrafine grain Mg–7.4%Al alloy synthesized by consolidation of mechanically alloyed powders. *J. Alloys Compd.* **610**, 456 (2014).

56. P. Molaiyan and R. Witter: Mechanochemical synthesis of solid-state electrolyte $Sm_{1−x}Ca_xF_{3−x}$ for batteries and other electrochemical devices. *Mater. Lett.* **244**, 22 (2019).

57. K.G. Prashanth and B.S. Murty: Production, kinetic study and properties of Fe-based glass and its composites. *Mater. Manuf. Process.* **25**, 592 (2010).

58. P. Susila, D. Sturm, M. Heilmaier, B.S. Murty, and V.S. Sarma: Effect of yttria particle size on the microstructure and compression creep properties of nanostructured oxide dispersion strengthened ferritic $(Fe–12Cr–2W–0.5Y_2O_3)$ alloy. *Mater. Sci. Eng. A* **528**, 4579 (2011).

59. K.G. Prashanth, S. Scudino, K.B. Surreddi, M. Sakaliyska, B.S. Murty, and J. Eckert: Crystallization kinetics of $Zr_{65}Ag_5Cu_{12.5}Ni_{10}Al_{7.5}$ glassy powders produced by ball milling of pre-alloyed ingots. *Mater. Sci. Eng. A* **513**, 279 (2009).

60. X. Liu, L. Zhang, and Y. Xu: Microstructure and mechanical properties of graphene reinforced $Fe_{50}Mn_{30}Co_{10}Cr_{10}$ high-entropy alloy composites synthesized by MA and SPS. *Appl. Phys. A* **123**, 567 (2017).

61. P. Molaiyan and R. Witter: Crystal phase and surface defect driven synthesis of $Pb_{1−x}Sn_xF_2$ solid solution electrolyte for fluoride ion batteries. *J. Electroanal. Chem.* **845**, 154–159 (2019).

62. P.V. Satyanarayana, R. Sokkalingam, P.K. Jena, K. Sivaprasad, and K.G. Prashanth: Tungsten matrix composite reinforced with CoCrFeMnNi high-entropy alloy: Impact of processing routes on microstructure and mechanical properties. *Metals* **9**, 992 (2019).

63. O. Guillon, J. Gonzalez-Julian, B. Dargatz, T. Kessel, G. Schierning, J. Rathel, and M. Herrmann: Field-assisted sintering technology/spark plasma sintering: Mechanisms, materials, and technology developments. *Adv. Eng. Mater.* **16**, 830 (2014).

64. Z.Y. Hu, Z.H. Zhang, X.W. Cheng, F.C. Wang, Y.F. Zhang, and S.L. Li: A review of multi-physical fields induced phenomena and effects in spark plasma sintering: Fundamentals and applications. *Mater. Des.* **191**, 108662 (2020).

65. W. Ji, W. Wang, H. Wang, J. Zhang, Y. Wang, F. Zhang, and Z. Fu: Alloying behavior and novel properties of CoCrFeNiMn high-entropy alloy fabricated by mechanical alloying and spark plasma sintering. *Intermetallics* **56**, 24 (2015).

66. Y.A. Alshataif, S. Sivasankaran, F.A. Al-Mufadi, A.S. Alaboodi, and H.R. Ammar: Synthesis, structure, and mechanical response of $Cr_{0.26}Fe_{0.24}Al_{0.5}$ and $Cr_{0.15}Fe_{0.14}Al_{0.30}Cu_{0.13}Si_{0.28}$ nanocrystallite entropy alloys. *Adv. Powder Technol.* **31**, 2161 (2020).

67. Y.L. Chen, Y.H. Hu, C.A. Hsieh, J.W. Yeh, and S.K. Chen: Competition between elements during mechanical alloying in an octonary multi-principal-element alloy system. *J. Alloys Compd.* **481**, 768 (2009).

68. Y. Xie, H. Cheng, Q. Tang, W. Chen, W. Chen, and P. Dai: Effects of N addition on microstructure and mechanical properties of CoCrFeNiMn high entropy alloy produced by mechanical alloying and vacuum hot pressing sintering. *Intermetallics* **93**, 228 (2018).

69. S. Praveen, A. Anupam, T. Sirasani, B.S. Murty, and R.S. Kottada: Characterization of oxide dispersed AlCoCrFe high entropy alloy synthesized by mechanical alloying and spark plasma sintering. *Trans. Indian Inst. Met.* **66**, 369 (2013).

70. S. Praveen, A. Anupam, R. Tilak, and R.S. Kottada: Phase evolution and thermal stability of AlCoCrFe high entropy alloy with carbon as unsolicited addition from milling media. *Mater. Chem. Phys.* **210**, 57 (2018).

71. H. Cheng, W. Chen, X. Liu, Q. Tang, Y. Xie, and P. Dai: Effect of Ti and C additions on the microstructure and mechanical properties of the FeCoCrNiMn high-entropy alloy. *Mater. Sci. Eng. A* **719**, 192 (2018).

72. R.M. Pohan, B. Gwalani, J. Lee, T. Alam, J.Y. Hwang, H.J. Ryu, R. Banerjee, and S.H. Hong: Microstructures and mechanical properties of mechanically alloyed and spark plasma sintered Al$_{0.3}$CoCrFeMnNi high entropy alloy. *Mater. Chem. Phys.* **210**, 62 (2018).

73. M. Vaidya, G.M. Muralikrishna, and B.S. Murty: High-entropy alloys by mechanical alloying: A review. *J. Mater. Res.* **34**, 664 (2019).

74. L. Rogal, Z. Szklarz, P. Bobrowski, D. Kalita, G. Garzeł, A. Tarasek, M. Kot, and M. Szlezynger: Microstructure and mechanical properties of Al–Co–Cr–Fe–Ni base high entropy alloys obtained using powder metallurgy. *Met. Mater. Int.* **25**, 930 (2019).

75. D. Wen, B. Jiang, Q. Wang, F. Yu, X. Li, R. Tang, R. Zhang, G. Chen, and C. Dong: Influences of Mo/Zr minor-alloying on the phase precipitation behavior in modified 310S austenitic stainless steels at high temperatures. *Mater. Des.* **128**, 34 (2017).

76. F. Peyrouzet, D. Hachet, R. Soulas, C. Navone, S. Godet, and S. Gorsse: Selective laser melting of Al$_{0.3}$CoCrFeNi high-entropy alloy: Printability, microstructure, and mechanical properties. *JOM* **71**, 3443 (2019).

77. Y.A. Alshataif, S. Sivasankaran, F.A. Al-Mufadi, A.S. Alaboodi, and H.R. Ammar: Manufacturing methods, microstructural and mechanical properties evolutions of high-entropy alloys: A review. *Met. Mater. Int.* **26**, 1099 (2020).

78. R. Sriharitha, B.S. Murty, and R.S. Kottada: Thermal stability and strengthening in spark plasma sintered Al$_x$CoCrCuFeNi high entropy alloys. *J. Alloys Compd.* **583**, 419 (2014).

79. B. Gwalani, R.M. Pohan, J. Lee, B. Lee, R. Banerjee, H.J. Ryu, and S.H. Hong: High-entropy alloy strengthened by in situ formation of entropy-stabilized nano-dispersoids. *Sci. Rep.* **8**, 14085 (2018).